

Anatomy of plasmons in generic Luttinger semimetals

Jing Wang*

*Department of Physics & Tianjin Key Laboratory of Low Dimensional Materials Physics and Preparing Technology,
Tianjin University, Tianjin 300072, People's Republic of China*

Ipsita Mandal†

*Department of Physics, Shiv Nadar Institution of Eminence (SNIOE),
Gautam Buddha Nagar, Uttar Pradesh 201314, India*

We investigate the parameter regimes favourable for the emergence of plasmons in isotropic, anisotropic, and band-mass symmetric and asymmetric Luttinger semimetals (LSMs). An LSM harbours a quadratic band-crossing point (QBCP) in its bandstructure, where the upper and lower branches of dispersion are doubly degenerate. While a nonzero temperature (T) can excite particle-hole pairs about the Fermi level due to thermal effects (even at zero doping), a finite doping (μ) sets the Fermi level away from the QBCP at any T , leading to a finite Fermi surface (rather than a Fermi point). Both these conditions naturally give rise to a finite density of states. A nonzero value of T or μ is thus a necessary condition for a plasmon to exist, as otherwise the zero density of states at the QBCP can never lead to the appearance of this collective mode. In addition to T and μ , we consider the effects of all possible parameters like cubic anisotropy, band-mass asymmetry, and a material-dependent variable X that is proportional to the mass (of the quasiparticle) and the number of fermion flavours. We implement a random-phase-approximation to compute the quasiparticle decay rate τ^{-1} (also known as the inelastic scattering rate) resulting from screened Coulomb interactions. A well-defined sharp peak in the profile of τ^{-1} signals the appearance of a plasmon. From our results, we conclude that X turns out to be a crucial tuning parameter, as higher values of X assist in the emergence of plasmons. On the other hand, the features are broadly insensitive to cubic anisotropy and band-mass asymmetry.

Contents

I. Introduction	1
II. Model	2
III. Bare polarization bubble	3
IV. Criteria for emergence of plasmons	5
A. Isotropic case	6
B. Anisotropic and band-mass asymmetric cases	7
V. Signature of plasmons from inelastic scattering rates	8
VI. Quasiparticle characteristics	10
VII. Summary and discussions	12
A. Appendix: Details for obtaining the one-loop polarization function	14
1. Isotropic LSM	14
2. Anisotropic and band-mass asymmetric LSMs	15
References	16

I. Introduction

In contemporary research, three-dimensional (3d) semimetals with a quadratic band-crossing point (QBCP) are being extensively studied [1–15]. Distinct from Dirac/Weyl semimetals possessing band-crossings with linear energy dispersions [16], such a bandstructure can be realized in materials like pyrochlore iridates $A_2Ir_2O_7$ (where A is a lanthanide

* E-mail: jing_wang@tju.edu.cn

† E-mail: ipsita.mandal@gmail.com

element [17, 18]), gray tin (α -Sn) [19, 20], and HgTe [21]. Such systems are also known as Luttinger semimetals (LSMs), since the Luttinger Hamiltonian of inverted band-gap semiconductors describes the low-energy physics [22–24].

Long-ranged Coulomb interactions in LSMs cause a quantum phase transition to a non-Fermi liquid state, dubbed as the Luttinger-Abrikosov-Beneslavskii (LAB) phase [1, 25], when the chemical potential is tuned to cut right at the band-crossing point¹. The possibility of the emergence of plasmons at a finite temperature [10] or chemical potential has also been explored [32, 33] in isotropic LSMs. One might wonder whether the fate of these plasmons are robust in the presence of anisotropies, which is a more natural possibility. To this end, in this paper, we compute the behaviour of plasmons for both isotropic and anisotropic LSMs, under the influence of both finite temperature (T) and doping (away from the QBCP). We also include the effects of band-mass asymmetries between the upper and lower bands.

We follow the strategy of treating screened Coulomb interactions in the 3d QBCP within a random-phase-approximation (RPA), as is done in Ref. [10]. In the first step, the real and imaginary parts of the bare polarization function (i.e. without any interaction line in the loop) are explicitly derived, and the results tell us if a plasmon mode can exist when we add Coulomb interactions to the system [cf. Eq. (12)]. For the sake of completeness, all external variables, including the frequencies and momenta are considered at the same footing. In addition to keeping T and chemical potential (μ) finite, a suitable material-dependent parameter X is introduced, which can influence the emergence of plasmons². Finally, the results for polarization bubble in various regimes are used to calculate the inelastic scattering rate of the LSM quasiparticles due to Coulomb interactions. We investigate various parameter regimes to figure out when it is possible for plasmons to exist, and this is captured by sharp peaks in the inelastic scattering rates. We would like to point out that the deviations from isotropic LSM, by breaking rotational symmetry and introducing asymmetry between the band masses of the upper and lower branches of dispersion, only slightly modify the zeros of the real part of effective dielectric function, and cannot lead to the generation of plasmons in the absence of finite T and/or μ . This is to be expected as those asymmetries do not lead to a finite density of states at the band-crossing points (which is essential for plasmons to exist), other than making the dispersions anisotropic.

The paper is organized as follows. In Sec. II, we present the low-energy effective model for a generic LSM. Sec. III shows the computations of the bare polarization bubble. In Sec. IV, we treat the Coulomb interaction within RPA, and figure out the behaviour of the dielectric function, whose zeros capture the dispersions of the plasmons. Sec. V is devoted to calculating the inelastic scattering rate, as the presence of sharp peaks in the profile of this function indicates long-lived plasmons. We also compute the spectral function and the wavefunction renormalization (quasiparticle residue). All our computations encompass the isotropic, anisotropic, and band-mass symmetric and asymmetric scenarios. Finally, we end with a summary and discussion in Sec. VII.

II. Model

We consider a paramagnetic bandstructure, arising in a spin-orbit coupled system, for which the states near the center of the Brillouin zone (i.e., the Γ -point) transform under the symmetry group operations as the four spin states of a particle with angular momentum $j = 3/2$, and four bands cross at that point. The corresponding angular momentum operators $\mathcal{J} = \{\mathcal{J}_1, \mathcal{J}_2, \mathcal{J}_3\}$ transform as the T_2 representation of the cubic group. The low-energy effective continuum model near the band-touching point is obtained from the $\mathbf{k} \cdot \mathbf{p}$ theory, and is captured by the Luttinger Hamiltonian [1, 22, 24]

$$\mathcal{H}_0 = \left(\frac{\alpha \mathbf{p}^2}{2m} - \mu \right) \Gamma_0 + \sum_{a=1}^5 d_a(\mathbf{p}) \Gamma_a + \eta \sum_{a=1}^5 s_a d_a(\mathbf{p}) \Gamma_a, \quad (1)$$

at chemical potential μ . Here, the set of five matrices $\{\Gamma_a\}$ gives the rank-four irreducible representation of the Euclidean Clifford algebra, satisfying anticommutation relation $\{\Gamma_a, \Gamma_{a'}\} = 2\delta_{aa'}$. In 3d, the basis for a generic 4×4 Hermitian matrix is constituted by the identity matrix (denoted by Γ_0) and the five $\{\Gamma_a\}$ matrices (with $a \in [1, 5]$). From the latter, we get ten more distinct matrices defined by $\Gamma_{ab} = \frac{1}{2i}[\Gamma_a, \Gamma_b]$. The three components of the spin operator \mathcal{J} can be expressed in terms of the Γ_{ab} -matrices via linear relations [1]. The functions denoted by $d_a(\mathbf{p})$ are the $\ell = 2$ spherical harmonics given by [6, 10, 34]

$$\begin{aligned} d_1(\mathbf{p}) &= \frac{\sqrt{3} p_y p_z}{2m}, & d_2(\mathbf{p}) &= \frac{\sqrt{3} p_x p_z}{2m}, & d_3(\mathbf{p}) &= \frac{\sqrt{3} p_x p_y}{2m}, \\ d_4(\mathbf{p}) &= \frac{\sqrt{3} (p_x^2 - p_y^2)}{4m}, & d_5(\mathbf{p}) &= \frac{2p_z^2 - p_x^2 - p_y^2}{4m}. \end{aligned} \quad (2)$$

The Γ_a -matrices can always be chosen such that three are real and two are imaginary [34]. We choose a representation in which $\{\Gamma_1, \Gamma_2, \Gamma_3\}$ are real and $\{\Gamma_4, \Gamma_5\}$ are imaginary. Using the same conventions as in Ref. [6], we set (i) $s_a = 1$ for

¹ In the presence of electron-electron interactions, when the Fermi level is away from the band-crossing point, it has been predicted that two-dimensional (2d) counterparts of the LSMs are unstable to interaction-driven topological insulating phases [26–31].

² Plasmons cannot exist at $T = \mu = 0$ because of the vanishing of density of states at the QBCP.

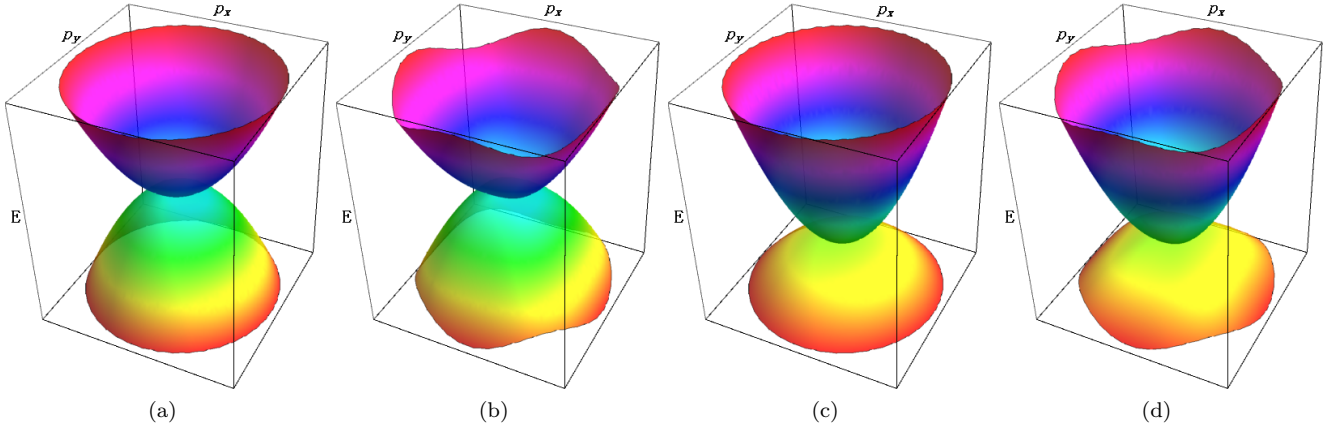


FIG. 1. Schematic dispersions of the Luttinger semimetals in the p_x - p_y plane for (a) $\alpha = 0$ and $\eta = 0$; (b) $\alpha \neq 0$ and $\eta = 0$; (c) $\alpha = 0$ and $\eta \neq 0$; and (d) $\alpha \neq 0, \eta \neq 0$.

the off-diagonal (i.e., for $a = \{2, 3, 4\}$); and (ii) $s_a = -1$ for the diagonal (i.e., for $a = \{1, 5\}$) Γ_a -matrices. Furthermore, the parameters α and η are directly related to the Luttinger parameters [6], affecting the various symmetries of an LSM. More specifically, the band-mass and rotational symmetries are unbroken only when $\alpha = 0$ and $\eta = 0$, respectively. The schematic band dispersions about the QBCP are shown in Fig. 1. Since the two branches of dispersions must have opposite curvatures, we must have $0 \leq \alpha < 1$.

III. Bare polarization bubble

In this section, we will calculate the one-loop bare polarization bubble, which means that we will not include any interaction line in the one-loop diagram. While evaluating the results, we will express the energies/frequencies in units of Λ_0 , which is the inverse of the lattice cut-off. Hence, we use the variables $T = \tilde{T} \Lambda_0$, $m = \tilde{m} \Lambda_0$, and $\mu = \tilde{\mu} \Lambda_0$. According to the same logic, we use the momentum and frequency scalings, such as $q = \tilde{q} \Lambda_0$ (where $q \equiv |\mathbf{q}|$) and $\omega = \tilde{\omega} \Lambda_0$. In short, we will use tilde to denote the dimensionless quantities obtained from their dimensionful counterparts scaled by appropriate powers of Λ_0 .

In the Matsubara space, the bare polarization function can be written as

$$\Pi(i\omega_n, \mathbf{q}) = - \int \frac{d^3 \mathbf{p}}{(2\pi)^3} \int_{-\infty}^{\infty} \frac{d\epsilon_1}{2\pi} \int_{-\infty}^{\infty} \frac{d\epsilon_2}{2\pi} \text{Tr} \left[A^{(0)}(\epsilon_1, \mathbf{p}) A^{(0)}(\epsilon_2, \mathbf{p} + \mathbf{q}) \right] \left(\frac{1}{\beta} \sum_{\Omega_m} \frac{1}{i\Omega_m - \epsilon_1} \frac{1}{i\Omega_m + i\omega_n - \epsilon_2} \right), \quad (3)$$

where $A^{(0)}(\epsilon, \mathbf{p})$ denotes the bare fermion spectral function, ω_n represents the fermionic Matsubara frequency, Ω_m is the bosonic Matsubara frequency, and $\beta = 1/T$ (setting the Boltzmann constant $k_B = 1$).

For the isotropic case, the bare fermion propagator in the Matsubara space takes the simple form

$$G_0(i\omega_n, \mathbf{p}) = \frac{1}{(-i\omega_n - \mu) \Gamma_0 + \mathbf{d}(\mathbf{p}) \cdot \mathbf{\Gamma}}, \quad (4)$$

leading to

$$A^{(0)}(\epsilon, \mathbf{p}) = - \frac{\pi \text{sgn}(\epsilon + \mu) [\epsilon + \mu + \mathbf{d}(\mathbf{p}) \cdot \mathbf{\Gamma}]}{|\mathbf{d}(\mathbf{p})|} \sum_{\zeta=\pm} \delta(\epsilon + \mu + \zeta |\mathbf{d}(\mathbf{p})|). \quad (5)$$

Analytic continuation to real frequencies, after some tedious algebra (see Appendix A 1), gives

$$\frac{\text{Re} \Pi^R(\tilde{\omega}, \tilde{q}, \Theta, \Phi)}{\tilde{m} \Lambda_0^2} = \sum_{\zeta_1, \zeta_2=\pm 1} \mathcal{K}_{\zeta_1 \zeta_2}(\tilde{\omega}, \tilde{q}, \Theta, \Phi), \quad \frac{\text{Im} \Pi^R(\tilde{\omega}, \tilde{q}, \Theta, \Phi)}{\tilde{m} \Lambda_0^2} = \sum_{\zeta_1, \zeta_2=\pm 1} \mathcal{F}_{\zeta_1 \zeta_2}(\tilde{\omega}, \tilde{q}, \Theta, \Phi), \quad (6)$$

where Λ_0 is the inverse of the lattice cut-off, and the explicit expressions for the functions $\mathcal{K}_{\zeta_1 \zeta_2}$ and $\mathcal{F}_{\zeta_1 \zeta_2}$ have been shown in Eq. (A6). Here we have used the variables $\{\tilde{q}, \Theta, \Phi\}$ to denote the spherical polar coordinates, which are related to the Cartesian coordinates as

$$q_x = q \sin \Theta \cos \Phi, \quad q_y = q \sin \Theta \sin \Phi, \quad q_z = q \cos \Theta. \quad (7)$$

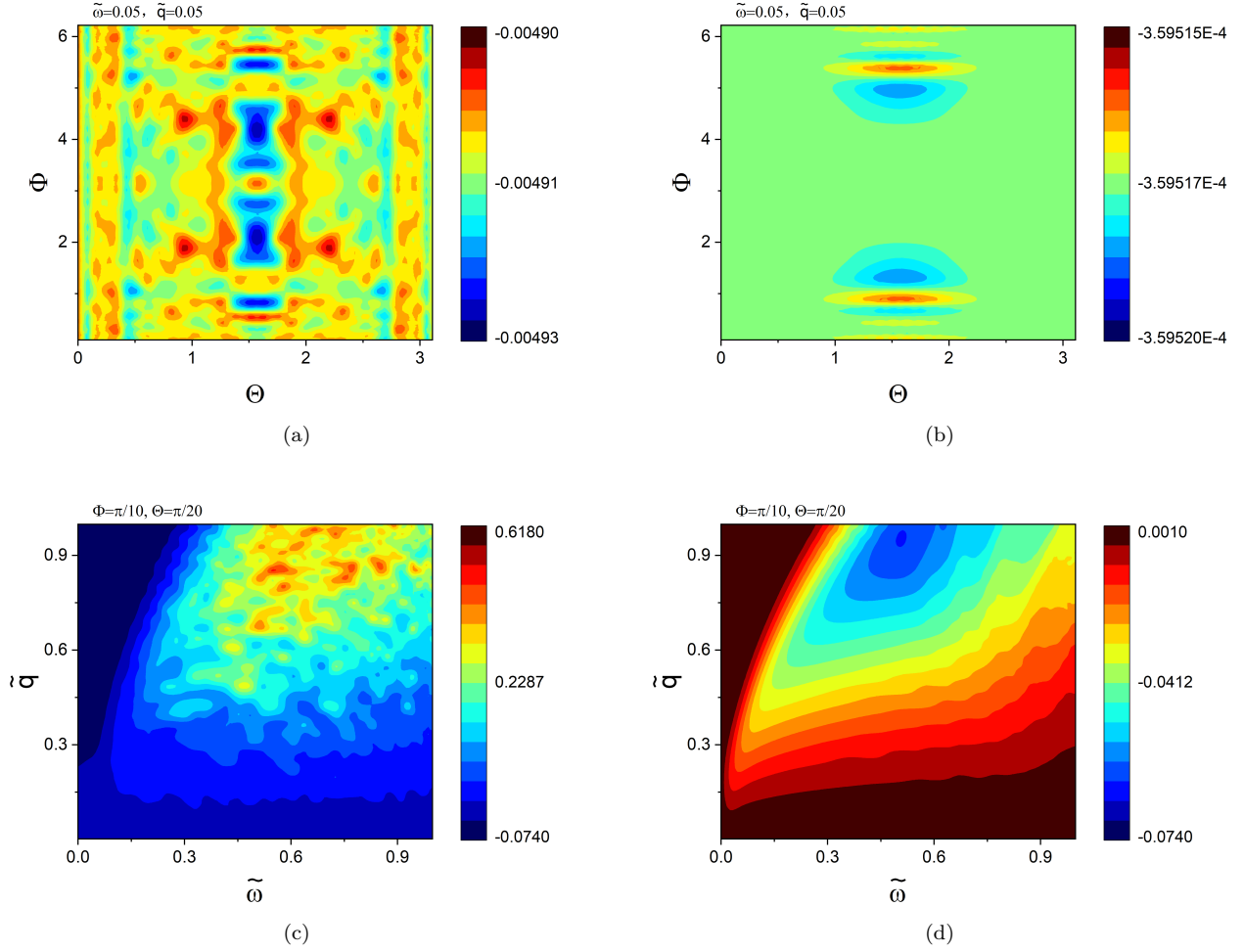


FIG. 2. Behaviour of the bare polarization function for an isotropic LSM with $\tilde{T} = 0.1$ and $\tilde{\mu} = 0.1$, and $\tilde{\omega}$ restricted to positive values: Subfigures (a) and (b) show the contourplots of $\tilde{m} \Lambda_0^2 \text{Re} \Pi^R$ and $\tilde{m} \Lambda_0^2 \text{Im} \Pi^R$, respectively, as functions of the angular variables Θ and Φ , for $\tilde{\omega} = 0.05$ and $\tilde{q} = 0.05$. Subfigures (c) and (d) show the contourplots of $\tilde{m} \Lambda_0^2 \text{Re} \Pi^R$ and $\tilde{m} \Lambda_0^2 \text{Im} \Pi^R$, respectively, as functions of $\tilde{\omega}$ and \tilde{q} , with $\Phi = \pi/10$ and $\Theta = \pi/20$.

For the anisotropic case, the bare fermionic propagator (in the Matsubara space) takes a bit more complicated form, captured by

$$G_0(i\omega_n, \mathbf{p}) = \frac{1}{\left(-i\omega_n + \frac{\alpha \mathbf{p}^2}{2m} - \mu\right) \Gamma_0 + \mathbf{d}(\mathbf{p}) \cdot \mathbf{\Gamma} + \eta \sum_{a=1}^5 s_a d_a(\mathbf{p}) \Gamma^a}, \quad (8)$$

such that the fermion spectral function is now given by

$$A^{(0)}(\epsilon) = -\pi \text{sgn}\left(\epsilon + \mu - \frac{\alpha \mathbf{p}^2}{2m}\right) \left[\epsilon + \mu - \frac{\alpha \mathbf{p}^2}{2m} + \mathbf{d}(\mathbf{p}) \cdot \mathbf{\Gamma} + \eta \sum_{a=1}^5 s_a d_a(\mathbf{p}) \Gamma^a \right] \times \frac{\sum_{\zeta=\pm} \delta\left(\epsilon + \mu - \frac{\alpha \mathbf{p}^2}{2m} + \zeta \sqrt{(1+\eta) \mathbf{d}^2(\mathbf{p}) + 2\eta \sum_{a'=1}^5 s_{a'} d_{a'}^2(\mathbf{p})}\right)}{\sqrt{(1+\eta) \mathbf{d}^2(\mathbf{p}) + 2\eta \sum_{b=1}^5 s_b d_b^2(\mathbf{p})}}. \quad (9)$$

The real and imaginary parts of the retarded polarization in this case are found to be

$$\frac{\text{Re} \Pi^R(\tilde{\omega}, \tilde{q}, \Theta, \Phi)}{\tilde{m} \Lambda_0^2} = \sum_{\zeta_1, \zeta_2 = \pm 1} \mathcal{M}_{\zeta_1 \zeta_2}(\tilde{\omega}, \tilde{q}, \Theta, \Phi), \quad \frac{\text{Im} \Pi^R(\tilde{\omega}, \tilde{q}, \Theta, \Phi)}{\tilde{m} \Lambda_0^2} = \sum_{\zeta_1, \zeta_2 = \pm 1} \mathcal{J}_{\zeta_1 \zeta_2}(\tilde{\omega}, \tilde{q}, \Theta, \Phi), \quad (10)$$

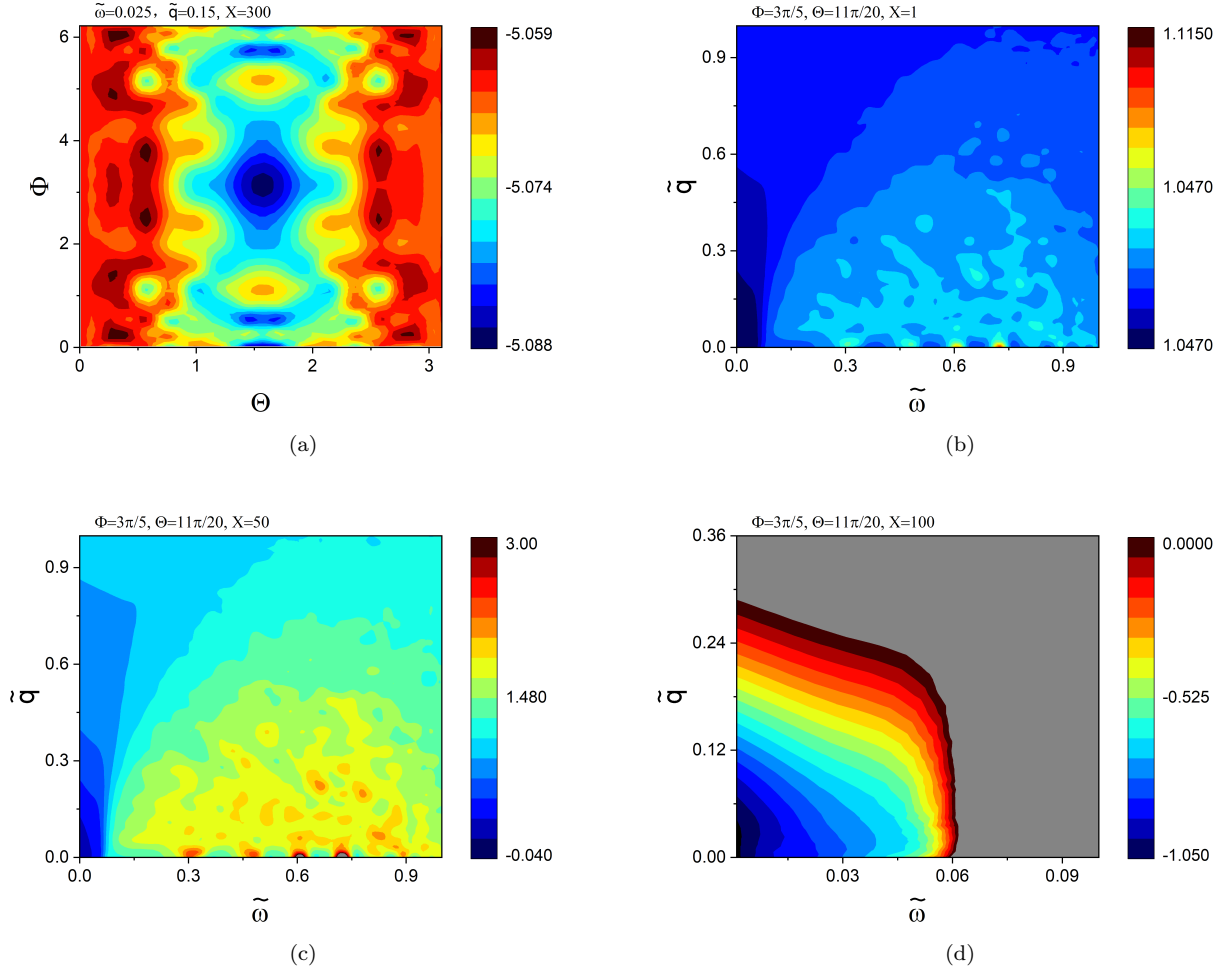


FIG. 3. Behaviour of $\text{Re } \mathcal{E}_{\text{eff}}$ for isotropic LSM with $\tilde{T} = 0.1$ and $\tilde{\mu} = 0.1$, and $\tilde{\omega}$ restricted to positive values: Subfigure (a) captures the dependence on the angular variables Θ and Φ , for $\tilde{\omega} = 0.025$, $\tilde{q} = 0.15$, and $X = 300$. Subfigures (b), (c), and (d) show the dependence on $\tilde{\omega}$ and \tilde{q} , with $\Phi = 3\pi/5$ and $\Theta = 11\pi/20$, for $X = 1$, $X = 50$, and $X = 100$, respectively.

where the explicit expressions for the functions $\mathcal{M}_{\zeta_1 \zeta_2}$ and $\mathcal{J}_{\zeta_1 \zeta_2}$ have been shown in Eq. (A9) of Appendix A 2. As in the isotropic case, we have used the spherical polar coordinates for these final expressions.

IV. Criteria for emergence of plasmons

We now include the effect of screened Coulomb interactions. Within RPA, this is captured by the effective interaction [10, 35]

$$V^R(\omega, \mathbf{q}) = \frac{V_0(\mathbf{q})}{1 + V_0(\mathbf{q}) N_f \Pi^R(\omega, \mathbf{q})}, \quad V_0(\mathbf{q}) = \frac{\alpha_0}{q^2} \equiv \frac{4\pi e^2}{\varepsilon q^2}, \quad (11)$$

where N_f is the number of fermion flavors, V_0 denotes the bare Coulomb interaction in a material with a dielectric constant ε , and e is the electron charge. In the literature, the coefficient e^2/ε is usually known as the effective fine structure constant.

The effective interaction $V^R(\omega, \mathbf{q})$ can be interpreted as the photon propagator in the given medium. If the function has any pole, that will indicate the emergence of a plasmon mode, resulting from collective photon-electron excitations. The dispersions of the plasmons are thus given by $[1 + V_0(\mathbf{q}) N_f \Pi^R(\omega, \mathbf{q})] = 0$, which are the zeros of the dielectric function

$$\mathcal{E}(\omega, \mathbf{q}) \equiv \varepsilon [1 + V_0(\mathbf{q}) N_f \Pi^R(\omega, \mathbf{q})]. \quad (12)$$

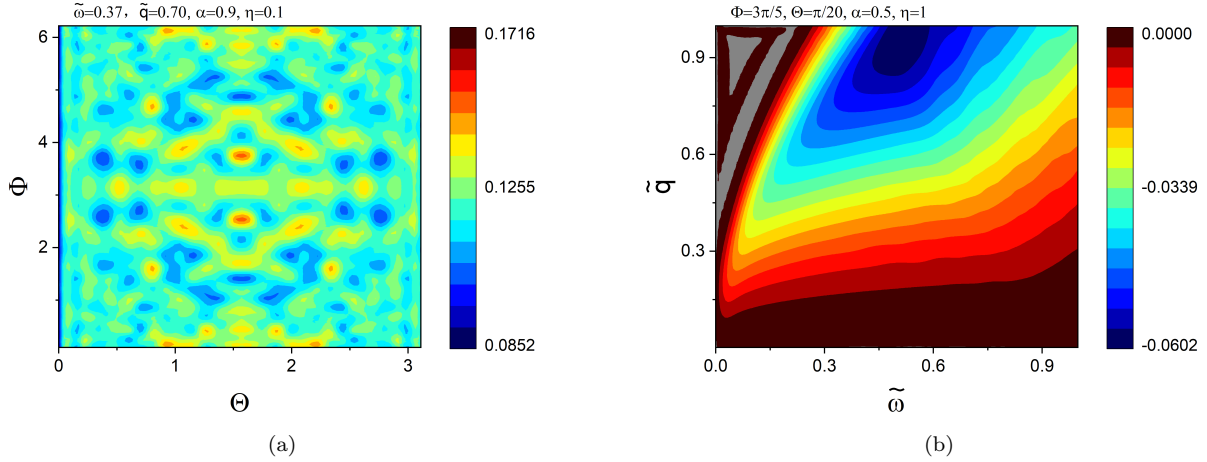


FIG. 4. Behaviour of the bare polarization function for a generic LSM with $\tilde{T} = 0.5$, $\tilde{\mu} = 0.1$, and $\tilde{\omega}$ restricted to positive values: Subfigure (a) shows $\tilde{m} \Lambda_0^2 \text{Re} \Pi^R$ as a function of Θ and Φ , for $\alpha = 0.9$, $\eta = 0.1$, $\tilde{\omega} = 0.37$, and $\tilde{q} = 0.7$. Subfigure (b) shows $\tilde{m} \Lambda_0^2 \text{Im} \Pi^R$ as a function of $\tilde{\omega}$ and \tilde{q} , for $\alpha = 0.5$, $\eta = 1$, $\Phi = 3\pi/5$, and $\Theta = 1\pi/20$.

For inconvenience, we break up the dielectric constant into real and imaginary parts as follows:

$$\frac{\mathcal{E}(\omega, \mathbf{q})}{\varepsilon} \equiv \text{Re} \mathcal{E}_{\text{eff}}(\omega, \mathbf{q}) + i \text{Im} \mathcal{E}_{\text{eff}}(\omega, \mathbf{q}), \quad \text{Re} \mathcal{E}_{\text{eff}}(\omega, \mathbf{q}) = 1 + \frac{N_f \alpha_0 \text{Re} \Pi^R(\omega, \mathbf{q})}{q^2}, \quad \text{Im} \mathcal{E}_{\text{eff}}(\omega, \mathbf{q}) = \frac{N_f \alpha_0 \text{Im} \Pi^R(\omega, \mathbf{q})}{q^2}. \quad (13)$$

The expression for the real part tells us that in order to have the possibility for the effective photon propagator V^R to have a pole, we must have regions where $\text{Re} \Pi^R < 0$. On the other hand, the imaginary part $\text{Im} \mathcal{E}_{\text{eff}}$ quantifies the decay rate of the plasmon mode. In all the following discussions, we use the definition

$$X \equiv N_f \alpha_0 \tilde{m}, \quad (14)$$

which is a material-dependent parameter, and we vary its value to investigate the regimes favourable for getting plasmons. We would like to clarify that although \tilde{m} is the scaled mass (and depends on the material we choose to employ in an experimental set-up), the number of fermion flavours N_f is a theoretical parameter, as the examples of materials mentioned in the paper will harbour a single band-touching point (implying $N_f = 1$). We keep N_f generic mainly for the reason that for the case of unscreened (or long-ranged) Coulomb interactions, one has to use some controlled approximation (as RPA fails in those cases). Dimensional regularization and large- N_f expansion [1, 25] are two alternate methods of controlled approximation. Hence, we have considered here a setting with N_f independent fermionic flavours, although the physical case corresponds to $N_f = 1$. In future, if we plan to investigate the emergence of plasmons for unscreened Coulomb interaction, keeping N_f generic will turn out to be handy.

A. Isotropic case

We show the behaviour of Π^R for some chosen parameter regimes in Fig. 2, by evaluating the associated integrals numerically. In all the plots, we use the values $\tilde{T} = 0.1$ and $\tilde{\mu} = 0.1$. We have checked that the qualitative behaviour for other parameter regimes (varying \tilde{T} and $\tilde{\mu}$ in the range $[0, 1]$) is similar to what we have presented here, and the basic conclusions are indeed unchanged irrespective of the concrete values of \tilde{T} and $\tilde{\mu}$ chosen. From the representative plots, we find that the behaviour is quite insensitive to the external angular variables, and is mostly affected by the magnitudes of \tilde{q} and $\tilde{\omega}$. Fig. 2(c) shows extended regions where $\text{Re} \Pi^R(\omega, \mathbf{q}) < 0$, and therefore have the potential to contribute to the emergence of plasmons.

We have checked extensively (covering other potential parameter regimes which are not shown here) that the frequency and momentum dependence of both the real and imaginary parts of the retarded polarization function are insensitive to the specific values of T and μ , as long as at least one of them is nonzero. Consequently, the regions with $\text{Re} \Pi^R(\omega, \mathbf{q}) < 0$ are very robust against the variations of both T and μ . In the regions where $\text{Re} \Pi^R(\omega, \mathbf{q}) < 0$, we find that $\text{Im} \Pi^R(\omega, \mathbf{q})$ has very small values for its magnitude (compared to that of $\text{Re} \Pi^R$), which indicates that the damping in these regions is likely to be very small (almost negligible), contributing to a long lifetime of the emergent plasmons.

Let us now investigate the features of the real part of the dielectric function \mathcal{E} . Since \mathcal{E} is related to Π^R by Eq. (12), its susceptibility to the changes in Φ and Θ is expected to be the same as that for Π^R . This is precisely what is seen in

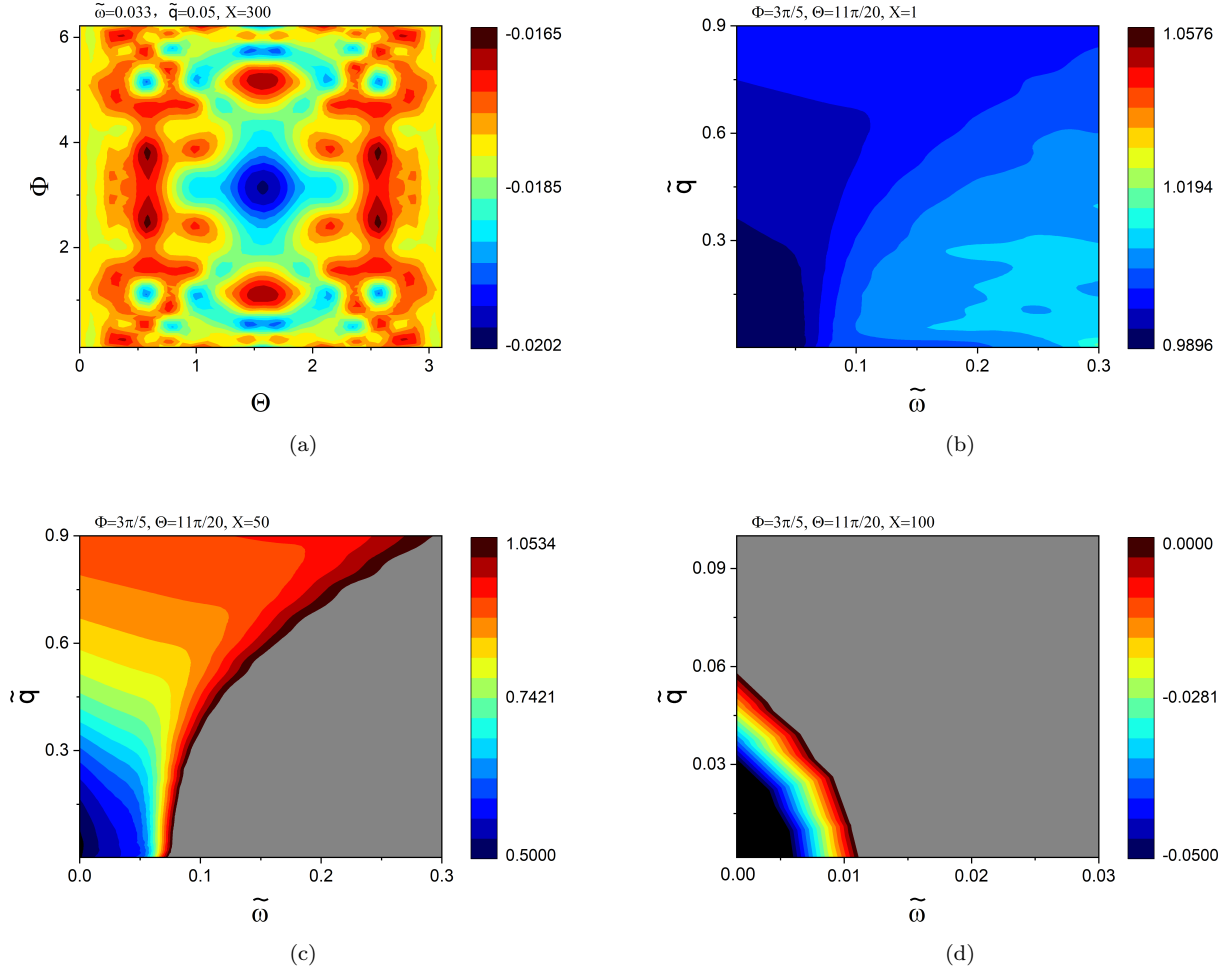


FIG. 5. Behaviour of $\text{Re } \mathcal{E}_{\text{eff}}$ for a generic LSM with $\tilde{T} = 0.5$, $\tilde{\mu} = 0.1$, and $\tilde{\omega}$ restricted to positive values: Subfigure (a) captures the dependence on the angular variables Θ and Φ , for $\alpha = 0.1$, $\eta = 1$, $\tilde{\omega} = 0.033$, $\tilde{q} = 0.05$, and $X = 300$. Subfigures (b), (c), and (d) show the dependence on $\tilde{\omega}$ and \tilde{q} , with $\Phi = 3\pi/5$ and $\Theta = 11\pi/20$, for $X = 1$, $X = 50$, and $X = 100$, respectively.

Fig. 3(a). Consequently, the key variable in substantially affecting the behaviour of \mathcal{E} is the material-dependent parameter X . The contours in Fig. 3(b)–(d) show that while for small values of X , $\text{Re } \mathcal{E}_{\text{eff}}(\omega, \mathbf{q})$ remain positive (i.e., do not possess any zeros), we obtain regions with zero and negative values when X is cranked up to higher values of the order of 50. Additionally, the regimes where $\text{Re } \mathcal{E}_{\text{eff}}(\omega, \mathbf{q})$ vanish get extended as X is increased. In analogy with the polarization function, we have also confirmed that the qualitative behaviour of $\text{Re } \mathcal{E}_{\text{eff}}(\omega, \mathbf{q})$ is stable against the variations of T and μ , as long as at least one of them is nonzero.

To summarize our observations, finite T and / or μ , and a suitable the material-dependent parameter X , create the possibility of obtaining plasmon poles in the isotropic LSMs. The former is a necessary requirement, while the latter provides a crucial tuning parameter.

B. Anisotropic and band-mass asymmetric cases

In this subsection, we investigate the effects of nonzero α and/or η , and show the results for $\tilde{T} = 0.5$ and $\tilde{\mu} = 0.1$. We have sampled the behaviour at other values of \tilde{T} and $\tilde{\mu}$ in the range $[0, 1]$, which is not shown here, as it does not show significant changes. Fig. 4 shows some plots in the regime $\alpha > \eta$. Although not shown here, we have extensively checked the characteristics for $\alpha = \eta$ and $\alpha < \eta$ as well, and have found that they are analogous to the cases presented here. Although the values of both the real and imaginary parts of the polarization function are slightly altered by the presence of finite anisotropic parameters, we have found that they are almost insensitive to the angular variables Φ and Θ . A representative plot is shown in Fig. 4. We also observe that the magnitude of $\text{Im } \Pi^R(\omega, \mathbf{q})$ is much smaller than that of $\text{Re } \Pi^R(\omega, \mathbf{q})$, in the regimes where the latter is negative.

The real part of the dielectric function \mathcal{E} follows the trends seen for Π^R (cf. Fig. 5), as far as the dependence on \tilde{T} ,

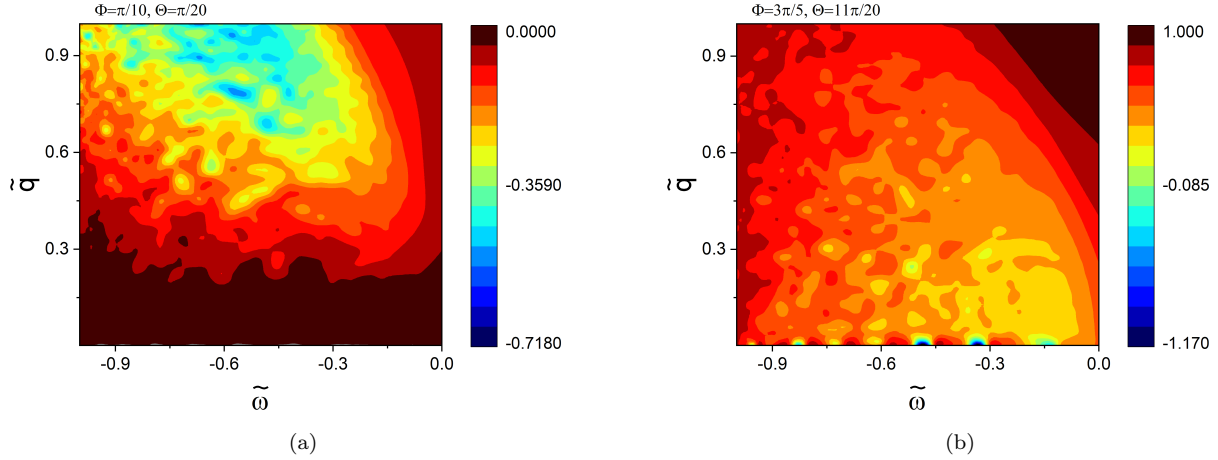


FIG. 6. Behaviour of (a) $\tilde{m} \Lambda_0^2 \text{Re}\Pi^R$ and (b) $\text{Re}\mathcal{E}_{\text{eff}}$ for a generic LSM with $\tilde{T} = 0.5$, $\tilde{\mu} = 0.1$, $X = 100$, and $\tilde{\omega}$ restricted to negative values. The values of the other parameters are the same as used in Fig. 4 and we have shown only two cases with the aim of comparing the corresponding behaviour shown in those plots (which represent the $\tilde{\omega} > 0$ case). We have not shown the plots for $\tilde{\omega} < 0$ that are the counterparts of the remaining subfigures of Figs. 2 and 3, because the basic tendency is similar.

$\tilde{\mu}$, Θ , and ϕ are concerned, due to the relation in Eq. (12). More specifically, we note that the behaviour of $\text{Re}\mathcal{E}$ is quite insensitive to these variables. As a result, the key variable which can potentially affect the characteristics of $\text{Re}\mathcal{E}$ drastically is the material-dependent parameter X . The plots in Fig. 5(b)–(d) show that while for small values of X , $\text{Re}\mathcal{E}_{\text{eff}}(\omega, \mathbf{q})$ remains positive (i.e., does not possess any zeros), regions with zero and negative values appear when X is tuned to higher values of the order of 50. Additionally, the regimes where $\text{Re}\mathcal{E}_{\text{eff}}(\omega, \mathbf{q})$ vanish get extended as X is increased. For the sake of completeness, we also show the behaviour of $\text{Re}\Pi^R$ and $\text{Re}\mathcal{E}_{\text{eff}}$ in Fig. 6, when $\tilde{\omega}$ is restricted to negative values.

We would like to point out that we have examined the data obtained for η -values ranging from 0 to 100, in tandem with various choices for $\alpha \in [0, 1)$. The variations due to anisotropy are seen to saturate as η is raised to ~ 100 and, even then, those variations are not significantly different from the qualitative features outlined above. On the basis of our extensive numerical explorations, we thus conclude that cubic anisotropy and anisotropic band-masses do not substantially change the nature of the poles in the effective interaction, compared to the isotropic case discussed in the previous subsection.

V. Signature of plasmons from inelastic scattering rates

In this section, we calculate the inelastic electron scattering rate τ^{-1} , resulting from the screened Coulomb interactions, where τ parametrizes the average lifetime of the quasiparticles. This is obtained from the imaginary part of the retarded fermion self-energy Σ^R .

The one-loop correction to the self-energy, caused by the Coulomb interaction, is given by

$$\Sigma(i\omega_n, \mathbf{q}) = T \int \frac{d^3\mathbf{p}}{(2\pi)^3} \sum_{\Omega_m} V(i\Omega_m, \mathbf{q}) G_0(i\omega_n + i\Omega_m, \mathbf{p} + \mathbf{q}) \quad (15)$$

in the Matsubara space, where $V(i\Omega_m, \mathbf{q})$ is the Matsubara-frequency-dependent counterpart of the effective retarded interaction shown in Eq. (11). Analytic continuation to real frequencies leads to

$$\text{Im}\Sigma^R(\varepsilon, \mathbf{q}) = \frac{1}{4} \int \frac{d^3\mathbf{p}}{(2\pi)^3} \int_{-\infty}^{\infty} \frac{d\omega}{2\pi} B(\omega, \mathbf{p}) A^{(0)}(\varepsilon + \omega, \mathbf{p} + \mathbf{q}) \left[\coth\left(\frac{\omega}{2T}\right) + \tanh\left(\frac{\varepsilon + \omega}{2T}\right) \right], \quad (16)$$

where

$$B(\varepsilon, \mathbf{q}) \equiv -2 \text{Im}V^R(\varepsilon, \mathbf{q}) = \frac{-2V_0^2(\mathbf{q})N_f \text{Im}\Pi^R(\varepsilon, \mathbf{q})}{[1 + V_0(\mathbf{q})N_f \text{Re}\Pi^R(\varepsilon, \mathbf{q})]^2 + [V_0(\mathbf{q})N_f \text{Im}\Pi^R(\varepsilon, \mathbf{q})]^2} \quad (17)$$

is the bosonic spectral function.

Since the self-energy is a 4×4 matrix, it is convenient to parametrize it as

$$\Sigma^R(\varepsilon, \mathbf{p}) = \Sigma_s^R \Gamma_0 + \Sigma_v^R \mathbf{d}(\mathbf{p}) \cdot \boldsymbol{\Gamma}. \quad (18)$$

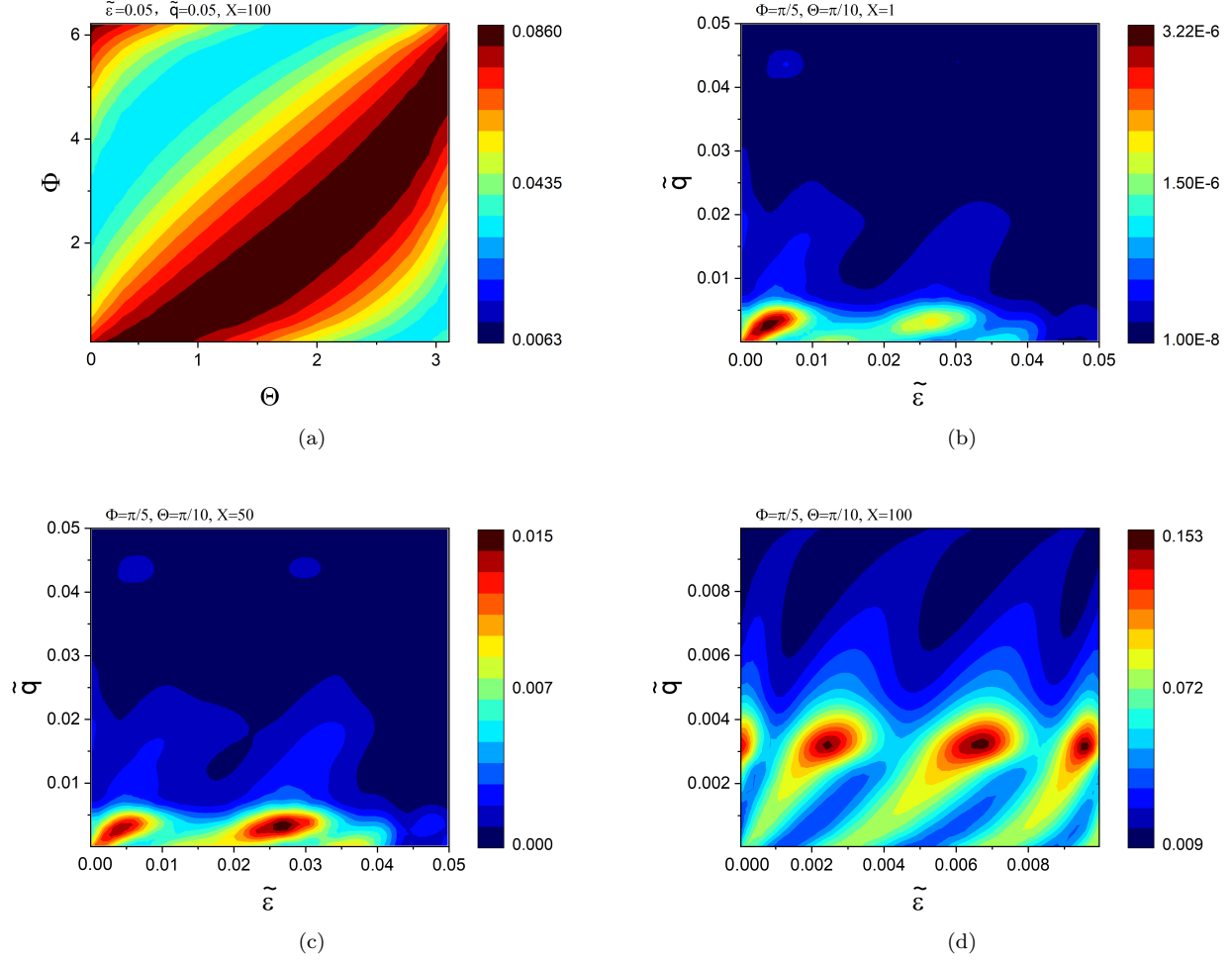


FIG. 7. Behaviour of $1/\tau$ for an isotropic LSM with $\tilde{T} = 0.1$, $\tilde{\mu} = 0.1$, and $\tilde{\varepsilon} \geq 0$: Subfigure (a) captures the dependence on the angular variables Θ and Φ , for $\tilde{\varepsilon} = \tilde{q} = 0.05$ and $X = 100$. Subfigures (b), (c), and (d) show the dependence on $\tilde{\varepsilon}$ and \tilde{q} , with $\Phi = \pi/5$ and $\Theta = \pi/10$, for $X = 1$, $X = 50$, and $X = 100$, respectively.

One can show that the scattering rate involves only Σ_s^R , and hence we only compute $\text{Im} \Sigma_s^R$, which takes the form:

$$\begin{aligned}
& \text{Im} \Sigma_s^R(\varepsilon, \mathbf{p}) \\
&= -\frac{\pi}{4} \int \frac{d^3 \mathbf{q}}{(2\pi)^3} \int_{-\infty}^{\infty} \frac{d\omega}{2\pi} B(\omega, \mathbf{q}) \left[\coth\left(\frac{\omega}{2T}\right) + \tanh\left(\frac{\varepsilon + \omega}{2T}\right) \right] \left[\varepsilon + \omega + \mu - \frac{\alpha(\mathbf{p} + \mathbf{q})^2}{2m} \right] \text{sgn}\left(\varepsilon + \omega + \mu - \frac{\alpha(\mathbf{p} + \mathbf{q})^2}{2m}\right) \\
&\quad \times \frac{\sum_{\zeta=\pm} \delta\left(\varepsilon + \omega + \mu - \frac{\alpha(\mathbf{p} + \mathbf{q})^2}{2m} + \zeta \sqrt{(1 + \eta) d_{\mathbf{p} + \mathbf{q}}^2 + 2\eta \sum_{a'=1}^5 s_{a'} d_{a'}^2(\mathbf{p} + \mathbf{q})}\right)}{\sqrt{(1 + \eta) |\mathbf{d}(\mathbf{p} + \mathbf{q})|^2 + 2\eta \sum_{a=1}^5 s_a d_a^2(\mathbf{p} + \mathbf{q})}}
\end{aligned} \tag{19}$$

in general.

Using the relation [36]

$$\frac{1}{\tau(\varepsilon, \mathbf{q})} \equiv -2 \text{Im} \Sigma_s^R(\varepsilon, \mathbf{q}), \tag{20}$$

we compute the scattering rate τ . Due to band-mass anisotropy, in general, $\tau(\varepsilon, \mathbf{q})$ is different from $\tau(-\varepsilon, \mathbf{q})$. First, let us focus on the $\varepsilon \geq 0$ case. Armed with the results obtained for the polarization bubbles discussed in Sec. IV, we make a judicious choice of the parameter regimes to numerically compute τ^{-1} . Figs. 7 and 8 show some representative plots. Fig. 8 demonstrates the features for nonzero α and η , and includes the cases $\alpha > \eta$, $\alpha = \eta$, and $\alpha < \eta$. Corroborating our observations for the results for Π^R and $\text{Re} \mathcal{E}_{\text{eff}}$, we find that nonzero anisotropy parameters hardly bring about substantial

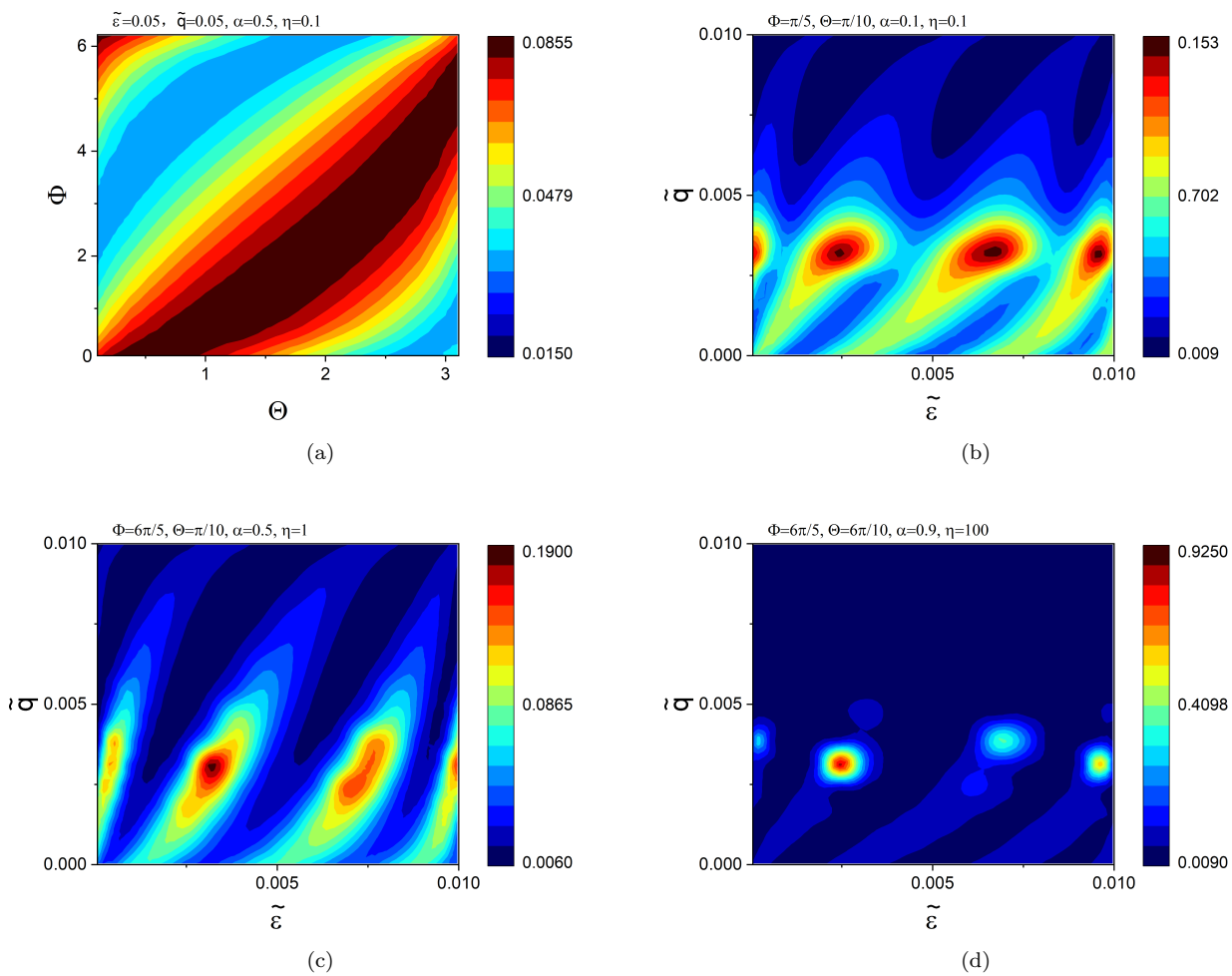


FIG. 8. Behaviour of $1/\tau$ for a generic LSM with $\tilde{T} = 0.5$, $\tilde{\mu} = 0.1$, $X = 100$, and $\tilde{\varepsilon} \geq 0$: Subfigure (a) captures the dependence on the angular variables Θ and Φ , for $\tilde{\varepsilon} = \tilde{q} = 0.05$, $\alpha = 0.5$, and $\eta = 0.1$. Subfigures (b), (c), and (d) show the dependence on $\tilde{\varepsilon}$ and \tilde{q} , for $\{\alpha, \eta, \Phi, \Theta\} = \{0.1, 0.1, \pi/5, \pi/10\}$, $\{\alpha, \eta, \Phi, \Theta\} = \{0.5, 1, 6\pi/5, \pi/10\}$, and $\{\alpha, \eta, \Phi, \Theta\} = \{0.9, 100, 6\pi/5, 6\pi/10\}$, respectively.

changes to the behaviour of $1/\tau$, compared to an isotropic LSM. Next, let us consider the $\varepsilon < 0$ case. Fig. 9 shows some representative plots for the isotropic scenario. We have checked that the basic results turn out to be similar when we consider the anisotropic case — hence, we have not shown those results here for the sake of brevity.

From the results shown in Figs. 7–9, we notice that the plasmon mode can be triggered more easily for the $\varepsilon > 0$ case than that for the $\varepsilon < 0$ case. We have explored various other parameter regimes (not shown in the plots presented here) similar to those pointed out in Sec. IV. Broadly, the features are found to be quite insensitive to variations in T , μ , α , and η . Of course, a higher value of X always favours the possibility of the emergence of plasmons.

VI. Quasiparticle characteristics

In this section, we investigate the behaviour of quasiparticle by computing the quasiparticle residue and spectral function at one-loop order [37] in the presence of the Coulomb interactions.

In the Matsubara space, the one-loop corrected fermionic propagator is given by [37]

$$G^{-1}(i\omega_n, \mathbf{p}) = G_0^{-1}(i\omega_n, \mathbf{p}) - \Sigma(i\omega_n, \mathbf{p}), \quad (21)$$

where $G_0(i\omega_n, \mathbf{p})$ is the bare fermion propagator defined in Eq. (4) or Eq. (8), depending on whether we are dealing with the isotropic or anisotropic case. Furthermore, $\Sigma(i\omega_n, \mathbf{p})$ is the one-loop fermionic self-energy, as defined in Eq. (15).

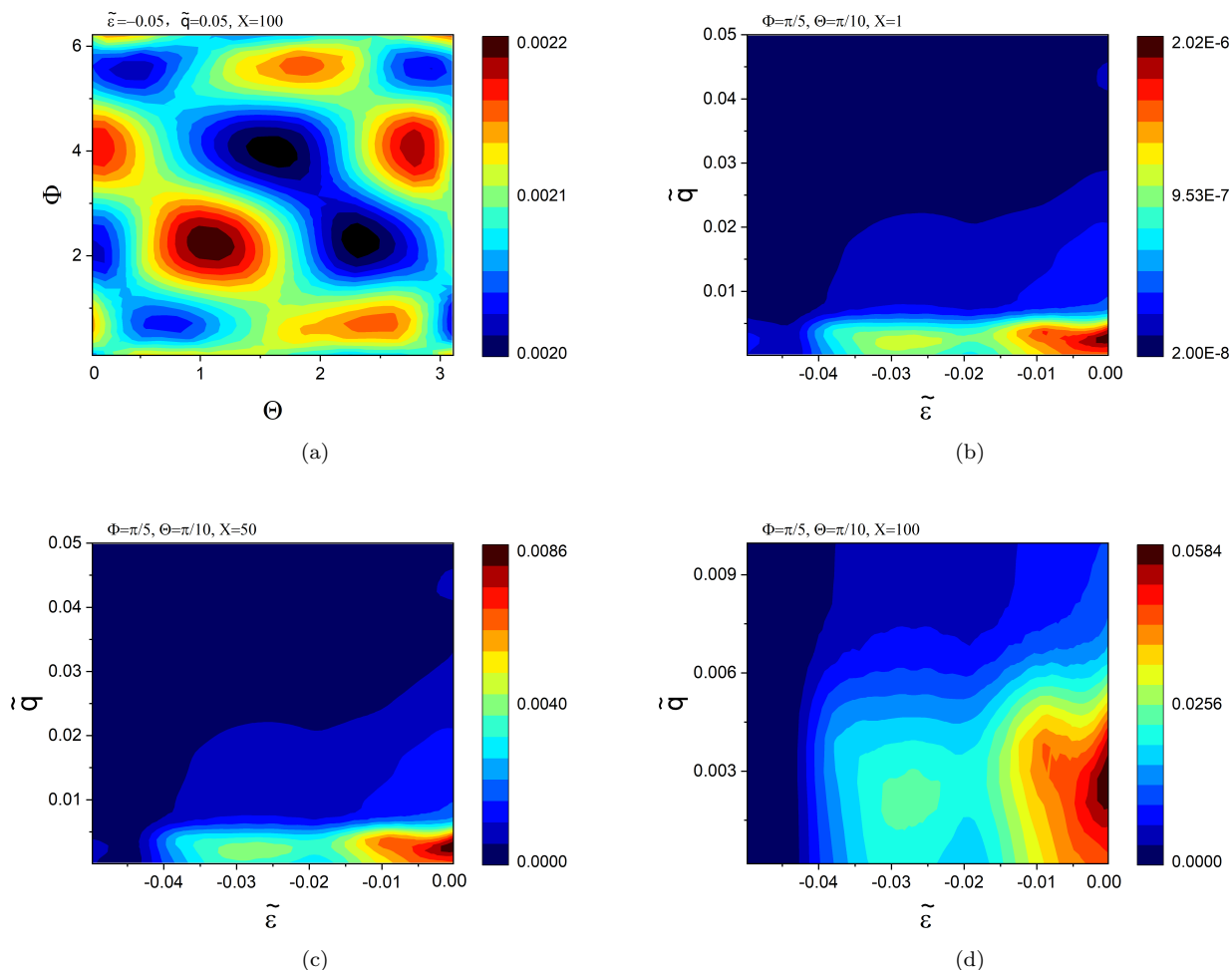


FIG. 9. Behaviour of $1/\tau$ for an isotropic LSM with $\tilde{T} = 0.1$, $\tilde{\mu} = 0.1$, and $\tilde{\varepsilon} < 0$: Subfigure (a) captures the dependence on the angular variables Θ and Φ , for $\tilde{\varepsilon} = -0.05$, $\tilde{q} = 0.05$, and $X = 100$. Subfigures (b), (c), and (d) show the dependence on $\tilde{\varepsilon}$ and \tilde{q} , with $\Phi = \pi/5$ and $\Theta = \pi/10$, for $X = 1$, $X = 50$, and $X = 100$, respectively.

Performing the appropriate analytic continuation to real frequencies, the retarded fermionic propagator can be written as

$$G^R(\omega, \mathbf{p}) = \frac{\left(-\omega + \frac{\alpha \mathbf{p}^2}{2m} - \mu\right) \Gamma_0 + \mathbf{d}(\mathbf{p}) \cdot \boldsymbol{\Gamma} + \eta \sum_{a=1}^5 s_a d_a(\mathbf{p}) \Gamma^a - \text{Re} \Sigma^R(\omega, \mathbf{p}) + i \text{Im} \Sigma^R(\omega, \mathbf{p})}{\left(-\omega + \frac{\alpha \mathbf{p}^2}{2m} - \mu - \text{Re} \Sigma^R(\omega, \mathbf{p})\right)^2 + \left[(1 + \eta) |\mathbf{d}(\mathbf{p})|^2 + 2\eta \sum_{a'=1}^5 s_{a'} (d_{a'}(\mathbf{p}))^2\right] + \{\text{Im} \Sigma^R(\omega, \mathbf{p})\}^2}. \quad (22)$$

This expressions leads to the one-loop corrected spectral function

$$A(\omega, \mathbf{q}) = -2 \text{Im} G^R(\omega, \mathbf{q}). \quad (23)$$

The Kramers-Kronig relation connects the real and imaginary parts of any complex function, such that

$$\text{Re} \Sigma^R(\omega, \mathbf{p}) = \int_{-\infty}^{\infty} \frac{d\omega'}{\pi} \frac{\text{Im} \Sigma^R(\omega', \mathbf{p})}{\omega' - \omega}, \quad (24)$$

which can be used for deriving $A(\omega, \mathbf{q})$, by plugging in the expression for $\text{Im} \Sigma^R$ shown in Eq. (16). Figs. 10 and 11 show some representative plots for the isotropic and anisotropic cases, respectively, for $\omega \geq 0$. The parameter values for these plots are the same as those in Figs. 7 and 8. Comparing Figs. 7 and 10 for an isotropic LSM, we find that the spectral function is strongly suppressed and gets saturated at the locations where peaks of $1/\tau$ are observed. This implies that quasiparticles are not even not well-defined in these regimes where plasmon modes are induced. For the anisotropic LSM, the basic tendencies are analogous, as seen from comparing Figs. 8 and 11. The results for the $\omega < 0$ case are again qualitatively similar, and hence not explicitly shown here.

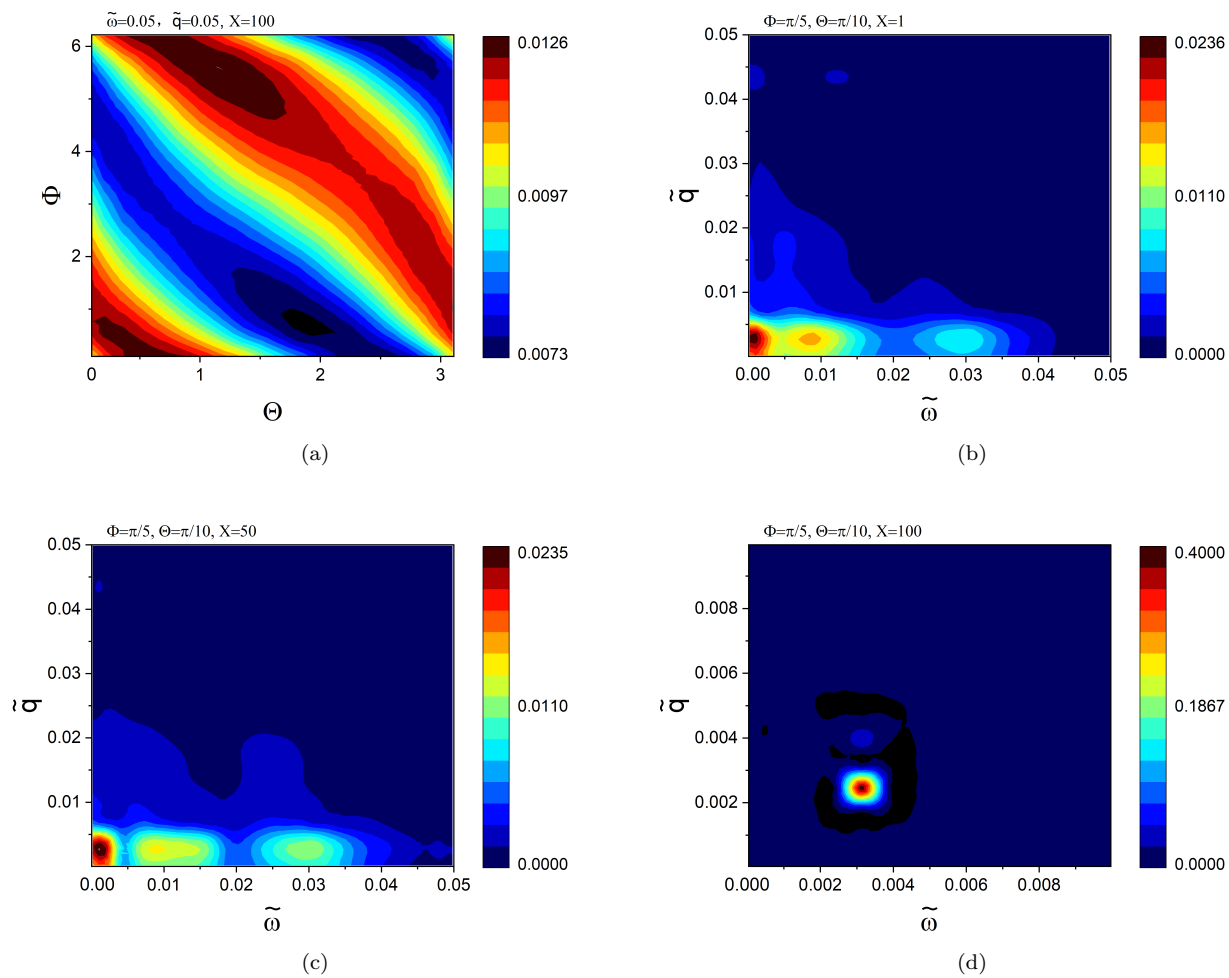


FIG. 10. Behaviour of the one-loop corrected spectral function A for an isotropic LSM with $\tilde{T} = 0.1$ and $\tilde{\mu} = 0.1$: Subfigure (a) captures the dependence on the angular variables Θ and Φ , for $\tilde{\omega} = \tilde{q} = 0.05$ and $X = 100$. Subfigures (b)–(d) show the dependence on $\tilde{\omega}$ and \tilde{q} , with $\Phi = \pi/5$ and $\Theta = \pi/10$, for $X = 1$, $X = 50$, and $X = 100$, respectively.

The quasiparticle weight is given by the residue at the pole of the Green's function, whose nonzero value signals the existence of the quasiparticles. This is captured by

$$Z_f(\mathbf{q}) = \frac{1}{1 - \lim_{\omega \rightarrow 0} \frac{\partial}{\partial \omega} \text{Re} \Sigma^R(\omega, \mathbf{q})}. \quad (25)$$

Fig. 12(a) is a representative contourplot of Z_f for an isotropic LSM, using the same parameter values as in Fig. 7 (except $\tilde{\varepsilon}$). A decrease in Z_f signals a reduction in the weight of the quasiparticle while the plasmon mode emerges. Furthermore, Fig. 12(b) clearly shows that Z_f decreases as X increases. This is due to the fact that the quasiparticles get destroyed and their weight is shifted to the plasmonic excitations as X is cranked up.

VII. Summary and discussions

To summarize, we have investigated the parameter regimes for the emergence of plasmons for isotropic, anisotropic, and band-mass symmetric and asymmetric Luttinger semimetals. A nonzero value of T or μ is a necessity to get a plasmon, as otherwise the zero density of states at the QBCP can never lead to the appearance of this collective mode. The action of a nonzero temperature is to excite particle-hole pairs about the Fermi level due to thermal effects (even at zero doping), creating the possibility of the emergence of thermal plasmons [10]. Needless to explain that a finite doping, on the other hand, sets the Fermi level away from the QBCP at any T , which naturally harbours a finite density of states.

We have also demonstrated the role of the material-dependent parameter $X = N_f \alpha_0 \tilde{m}$, which can favourably affect the emergence of plasmons. Although a nonzero T or μ is necessary for plasmons to materialize, we have found that the specific values of T and μ do not matter much, and the plasmons peaks are quite insensitive to a variation of these values.

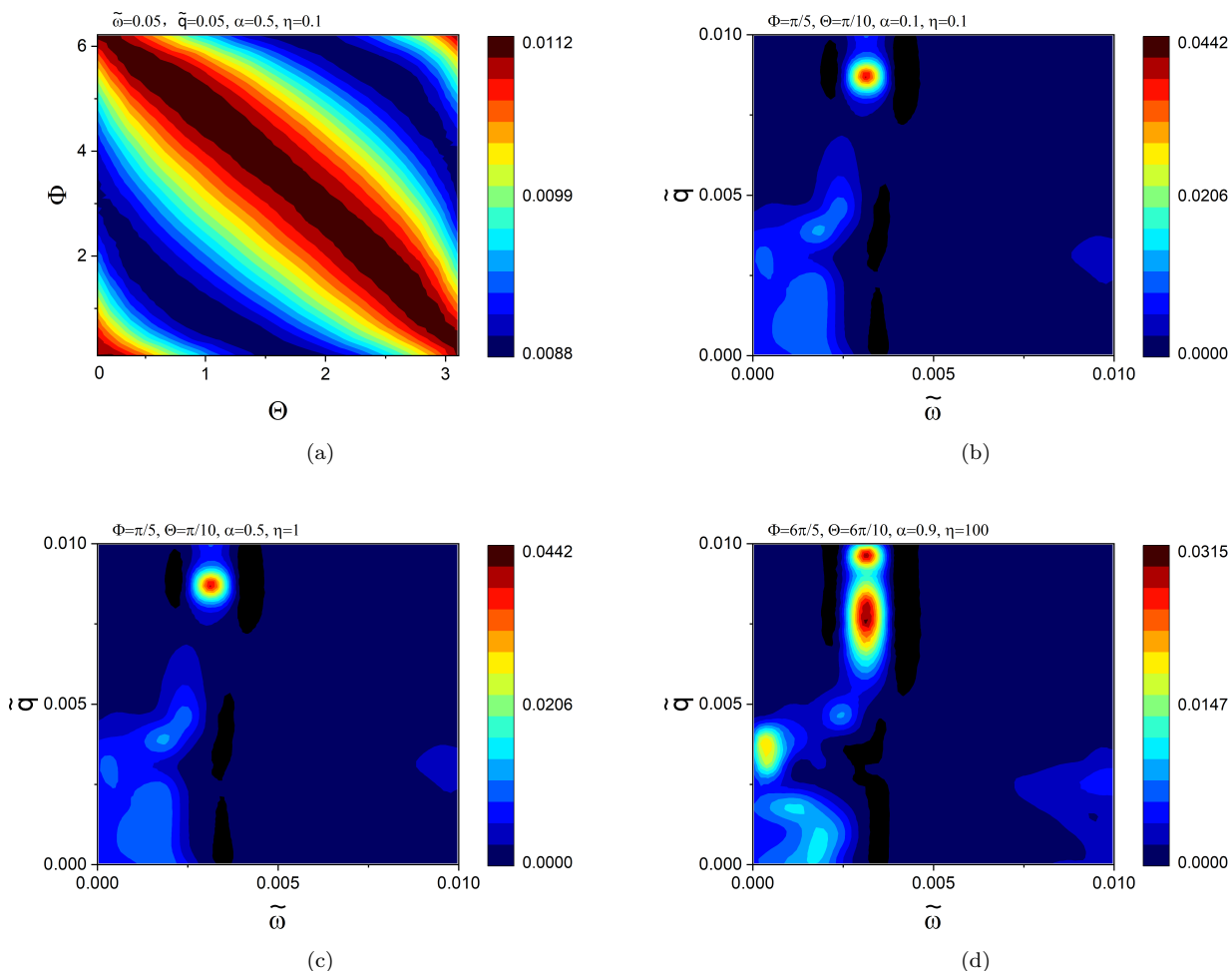


FIG. 11. Behaviour of the one-loop corrected spectral function A for a generic LSM with $\tilde{T} = 0.5$, $\tilde{\mu} = 0.1$, $X = 100$, and $\tilde{\omega} > 0$: Subfigure (a) captures the dependence on the angular variables Θ and Φ , for $\tilde{\omega} = \tilde{q} = 0.05$, $\alpha = 0.5$, and $\eta = 0.1$. Subfigures (b), (c), and (d) show the dependence on $\tilde{\omega}$ and \tilde{q} , for $\{\alpha, \eta, \Phi, \Theta\} = \{0.1, 0.1, \pi/5, \pi/10\}$, $\{\alpha, \eta, \Phi, \Theta\} = \{0.5, 1, \pi/5, \pi/10\}$, and $\{\alpha, \eta, \Phi, \Theta\} = \{0.9, 100, 6\pi/5, 6\pi/10\}$, respectively.

On the contrary, the parameter regimes for the existence of plasmon get broadened on increasing the value of X . Since X is proportional to the number of fermion flavours, it gives us a powerful tuning parameter to influence the existence of the plasmons in LSMs.

There are two important properties that are elucidated through our numerical results and plots: (1) decay rate τ^{-1} of the quasiparticles, and (2) quasiparticle weight or residue Z_f . The values of both these factors determine whether conditions are favourable for the existence of well-defined and long-lived plasmons or quasiparticles. The favourable conditions for one are detrimental to the other. These questions were studied earlier exclusively for isotropic LSMs in Refs. [10, 32, 33]. While Ref. [10] considered a finite T , Refs. [32, 33] examined the effects of finite doping at $T = 0$. Ref. [33] also took band-mass asymmetries into account. In this paper, we have considered the effects of nonzero values T and μ simultaneously. But the most important aspect of our computations is that we have considered generic LSM Hamiltonians, which include cubic anisotropies and band-mass asymmetries. These parameters are more likely to capture the features of realistic materials. Since it is not possible to get closed-form analytical approximations for the essential physical quantities in such a complicated system (not even for the retarded bare polarization bubble), we have obtained all our results by extensive numerical simulations. Our results will provide valuable information for future experiments engineered to measure transport or spectral properties of generic LSMs.

Acknowledgments

J.W. is grateful to Zhao-Kun Yang for helpful discussions on the implementation parallel computing, and has been partially supported by the National Natural Science Foundation of China under grant number 11504360.

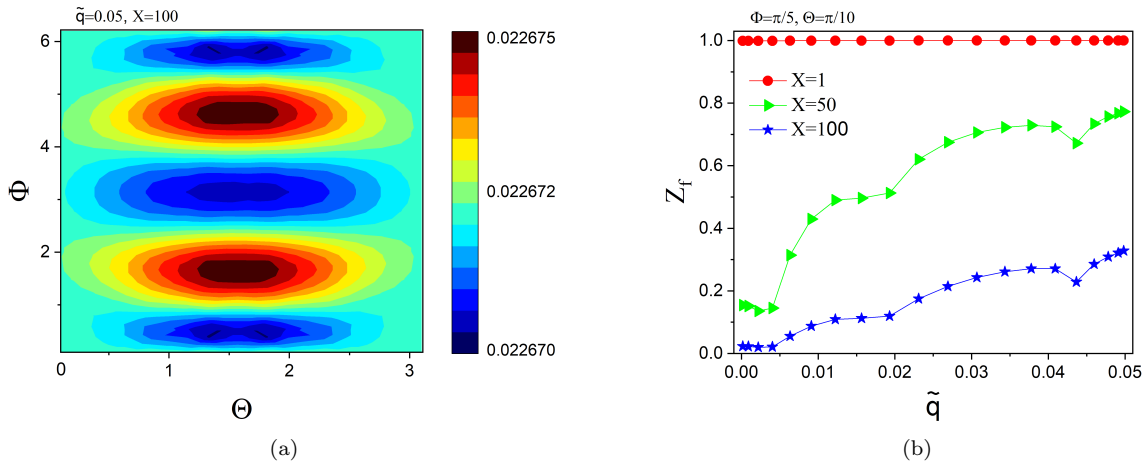


FIG. 12. Behaviour of Z_f for an isotropic LSM with $\tilde{T} = 0.1$ and $\tilde{\mu} = 0.1$: Subfigure (a) captures the dependence on the angular variables Θ and Φ , for $\tilde{q} = 0.05$ and $X = 100$. Subfigure (b) shows the dependence on \tilde{q} , with $\Phi = \pi/5$ and $\Theta = \pi/10$, for $X = 1$ (red), $X = 50$ (green), and $X = 100$ (blue).

Data availability statement

No data was used for the research described in the article.

Author contribution statement

I.M. conceived the original idea, developed the theory, and supervised the findings of this paper. J.W. performed the analytical calculations and the numerical simulations. All authors discussed the results and contributed to the final manuscript.

A. Appendix: Details for obtaining the one-loop polarization function

We will outline here some of the important intermediate steps for obtaining the expressions for the bare polarization bubbles, shown in Sec. III.

1. Isotropic LSM

Starting with Eq. (3), and using Eq. (4), we obtain

$$\begin{aligned} \Pi^R(\omega, \mathbf{q}) = & - \sum_{\zeta_1, \zeta_2 = \pm 1} \frac{\zeta_1 \zeta_2}{8} \int \frac{d^3 \mathbf{p}}{(2\pi)^3} \frac{\tanh \left[\frac{\beta \{ \zeta_1 |\mathbf{d}(\mathbf{p})| - \mu \}}{2} \right] - \tanh \left[\frac{\beta \{ \zeta_2 |\mathbf{d}(\mathbf{p} + \mathbf{q})| - \mu \}}{2} \right]}{\omega + \zeta_1 |\mathbf{d}(\mathbf{p})| - \zeta_2 |\mathbf{d}(\mathbf{p} + \mathbf{q})| + i0^+} \\ & \times \frac{\text{Tr} \left[\{ \zeta_1 |\mathbf{d}(\mathbf{p})| + \mathbf{d}(\mathbf{p}) \cdot \boldsymbol{\Gamma} \} \{ \zeta_2 |\mathbf{d}(\mathbf{p} + \mathbf{q})| + \mathbf{d}(\mathbf{p} + \mathbf{q}) \cdot \boldsymbol{\Gamma} \} \right]}{|\mathbf{d}(\mathbf{p})| |\mathbf{d}(\mathbf{p} + \mathbf{q})|}. \end{aligned} \quad (\text{A1})$$

For computational convenience, we switch to the spherical coordinates, using the relations

$$p_x = p \sin \theta \cos \phi, \quad p_y = p \sin \theta \sin \phi, \quad p_z = p \cos \theta, \quad (\text{A2})$$

and

$$q_x = q \sin \Theta \cos \Phi, \quad q_y = q \sin \Theta \sin \Phi, \quad q_z = q \cos \Theta. \quad (\text{A3})$$

Using the identity

$$\frac{1}{x - y + i0^+} = \mathcal{P} \left(\frac{1}{x - y} \right) - i\pi \delta(x - y), \quad (\text{A4})$$

and defining Λ_0 as the inverse of the lattice spacing, we get

$$\frac{\text{Re } \Pi^R(\tilde{\omega}, \tilde{q}, \Theta, \Phi)}{\tilde{m} \Lambda_0^2} = \sum_{\zeta_1, \zeta_2 = \pm 1} \mathcal{K}_{\zeta_1 \zeta_2}(\tilde{\omega}, \tilde{q}, \Theta, \Phi), \quad \frac{\text{Im } \Pi^R(\tilde{\omega}, \tilde{q}, \Theta, \Phi)}{\tilde{m} \Lambda_0^2} = \sum_{\zeta_1, \zeta_2 = \pm 1} \mathcal{F}_{\zeta_1 \zeta_2}(\tilde{\omega}, \tilde{q}, \Theta, \Phi). \quad (\text{A5})$$

The functions $\mathcal{K}_{\zeta_1 \zeta_2}$ and $\mathcal{F}_{\zeta_1 \zeta_2}$ are given by

$$\begin{aligned} & \mathcal{K}_{\zeta_1 \zeta_2}(\tilde{\omega}, \tilde{q}, \Theta, \Phi) \\ &= -\frac{\zeta_1 \zeta_2}{16 \pi^2} \int_0^1 d\tilde{p} \tilde{p}^2 \int_0^\pi d\theta \sin \theta \int_0^{2\pi} d\phi \left[\tanh\left(\frac{\zeta_1 |\boldsymbol{\eta}_{\mathbf{p}}| - \tilde{\mu}}{2\tilde{T}}\right) - \tanh\left(\frac{\zeta_2 |\boldsymbol{\eta}_{\mathbf{p}+\mathbf{q}}| - \tilde{\mu}}{2\tilde{T}}\right) \right] \left[|\boldsymbol{\eta}_{\mathbf{p}}| |\boldsymbol{\eta}_{\mathbf{p}+\mathbf{q}}| + \boldsymbol{\eta}_{\mathbf{p}} \cdot \boldsymbol{\eta}_{\mathbf{p}+\mathbf{q}} \right] \\ & \quad \times \mathcal{P}\left(\frac{1}{|\boldsymbol{\eta}_{\mathbf{p}}| |\boldsymbol{\eta}_{\mathbf{p}+\mathbf{q}}| (\tilde{\omega} - \zeta_1 |\boldsymbol{\eta}_{\mathbf{p}}| - \zeta_2 |\boldsymbol{\eta}_{\mathbf{p}+\mathbf{q}}|)}\right), \\ & \mathcal{F}_{\zeta_1 \zeta_2}(\tilde{\omega}, \tilde{q}, \Theta, \Phi) \\ &= \frac{\zeta_1 \zeta_2}{16 \pi^2} \int_0^1 d\tilde{p} \tilde{p}^2 \int_0^\pi d\theta \sin \theta \int_0^{2\pi} d\phi \left[\tanh\left(\frac{\zeta_1 |\boldsymbol{\eta}_{\mathbf{p}}| - \tilde{\mu}}{2\tilde{T}}\right) - \tanh\left(\frac{\zeta_2 |\boldsymbol{\eta}_{\mathbf{p}+\mathbf{q}}| - \tilde{\mu}}{2\tilde{T}}\right) \right] \\ & \quad \times \left(1 + \frac{\boldsymbol{\eta}_{\mathbf{p}} \cdot \boldsymbol{\eta}_{\mathbf{p}+\mathbf{q}}}{|\boldsymbol{\eta}_{\mathbf{p}}| |\boldsymbol{\eta}_{\mathbf{p}+\mathbf{q}}|} \right) \delta(\tilde{\omega} + \zeta_1 |\boldsymbol{\eta}_{\mathbf{p}}| - \zeta_2 |\boldsymbol{\eta}_{\mathbf{p}+\mathbf{q}}|), \end{aligned} \quad (\text{A6})$$

where

$$\tilde{m} = m/\Lambda_0, \quad \tilde{\omega} = \omega/\Lambda_0, \quad \tilde{\mu} = \mu/\Lambda_0, \quad \tilde{T} = T/\Lambda_0, \quad \tilde{q} = q/\Lambda_0, \quad \tilde{p} = p/\Lambda_0, \quad \boldsymbol{\eta}_{\mathbf{p}} = \frac{2m \mathbf{d}(\mathbf{p})}{\Lambda_0^2}. \quad (\text{A7})$$

2. Anisotropic and band-mass asymmetric LSMs

Following the same steps as outlined for the isotropic case in the previous subsection, and using Eq. (8), the expression in Eq. (3) now leads to

$$\frac{\text{Re } \Pi^R(\tilde{\omega}, \tilde{q}, \Theta, \Phi)}{\tilde{m} \Lambda_0^2} = \sum_{\zeta_1, \zeta_2 = \pm 1} \mathcal{M}_{\zeta_1 \zeta_2}(\tilde{\omega}, \tilde{q}, \Theta, \Phi), \quad \frac{\text{Im } \Pi^R(\tilde{\omega}, \tilde{q}, \Theta, \Phi)}{\tilde{m} \Lambda_0^2} = \sum_{\zeta_1, \zeta_2 = \pm 1} \mathcal{J}_{\zeta_1 \zeta_2}(\tilde{\omega}, \tilde{q}, \Theta, \Phi), \quad (\text{A8})$$

where

$$\begin{aligned} & \mathcal{M}_{\zeta_1 \zeta_2}(\tilde{\omega}, \tilde{q}, \Theta, \Phi) \\ &= -\frac{\zeta_1 \zeta_2}{16 \pi^2} \int_0^1 d\tilde{p} \tilde{p}^2 \int_0^\pi d\theta \sin \theta \int_0^{2\pi} d\phi \left[\tanh\left(\frac{\mathcal{B}_{\zeta_1}(\mathbf{p}) - \mu}{2T}\right) - \tanh\left(\frac{\mathcal{B}_{\zeta_2}(\mathbf{p} + \mathbf{q}) - \mu}{2T}\right) \right] \\ & \quad \times \mathcal{P}\left(\frac{\Lambda_0^4}{m^2 \mathcal{A}(\mathbf{p}) \mathcal{A}(\mathbf{p} + \mathbf{q})} \times \frac{1}{\tilde{\omega} + m \frac{\mathcal{B}_{\zeta_1}(\mathbf{p}) - \mathcal{B}_{\zeta_2}(\mathbf{p} + \mathbf{q})}{\Lambda_0^2}}\right) \\ & \quad \times \left\{ \zeta_1 \zeta_2 + \frac{(1 + \eta^2) \mathbf{d}(\mathbf{p}) \cdot \mathbf{d}(\mathbf{p} + \mathbf{q}) + 2\eta \sum_{a=1}^5 s_a d_a(\mathbf{p}) d_a(\mathbf{p} + \mathbf{q})}{\mathcal{A}(\mathbf{p}) \mathcal{A}(\mathbf{p} + \mathbf{q})} \right\}, \\ & \mathcal{J}_{\zeta_1 \zeta_2}(\tilde{\omega}, \tilde{q}, \Theta, \Phi) \\ &= \frac{\zeta_1 \zeta_2}{16 \pi^2} \int_0^1 d\tilde{p} \tilde{p}^2 \int_0^\pi d\theta \sin \theta \int_0^{2\pi} d\phi \left[\tanh\left(\frac{\mathcal{B}_{\zeta_1}(\mathbf{p}) - \mu}{2T}\right) - \tanh\left(\frac{\mathcal{B}_{\zeta_2}(\mathbf{p} + \mathbf{q}) - \mu}{2T}\right) \right] \delta\left(\tilde{\omega} + m \frac{\mathcal{B}_{\zeta_1}(\mathbf{p}) - \mathcal{B}_{\zeta_2}(\mathbf{p} + \mathbf{q})}{\Lambda_0^2}\right) \\ & \quad \times \left\{ \zeta_1 \zeta_2 + \frac{(1 + \eta^2) \mathbf{d}(\mathbf{p}) \cdot \mathbf{d}(\mathbf{p} + \mathbf{q}) + 2\eta \sum_{a=1}^5 s_a d_a(\mathbf{p}) d_a(\mathbf{p} + \mathbf{q})}{\mathcal{A}(\mathbf{p}) \mathcal{A}(\mathbf{p} + \mathbf{q})} \right\}, \end{aligned} \quad (\text{A9})$$

where

$$\mathcal{A}(\mathbf{p}) = \sqrt{(1 + \eta) \mathbf{d}^2(\mathbf{p}) + 2\eta \sum_{a=1}^5 s_a d_a^2(\mathbf{p})}, \quad \mathcal{B}_\zeta(\mathbf{p}) = \frac{\alpha \mathbf{p}^2}{2m} - \zeta \mathcal{A}(\mathbf{p}). \quad (\text{A10})$$

-
- [1] E.-G. Moon, C. Xu, Y. B. Kim, and L. Balents, Non-Fermi-liquid and topological states with strong spin-orbit coupling, *Phys. Rev. Lett.* **111**, 206401 (2013).
- [2] T. Kondo, M. Nakayama, R. Chen, J. J. Ishikawa, E. G. Moon, T. Yamamoto, Y. Ota, W. Malaeb, H. Kanai, Y. Nakashima, Y. Ishida, R. Yoshida, H. Yamamoto, M. Matsunami, S. Kimura, N. Inami, K. Ono, H. Kumigashira, S. Nakatsuji, L. Balents, and S. Shin, Quadratic Fermi node in a 3d strongly correlated semimetal, *Nature Communications* **6**, 10042 (2015).
- [3] B. Dóra and I. F. Herbut, Quadratic band touching with long-range interactions in and out of equilibrium, *Phys. Rev. B* **94**, 155134 (2016).
- [4] I. Boettcher and I. F. Herbut, Anisotropy induces non-Fermi-liquid behavior and nematic magnetic order in three-dimensional Luttinger semimetals, *Phys. Rev. B* **95**, 075149 (2017).
- [5] R. M. Nandkishore and S. A. Parameswaran, Disorder-driven destruction of a non-Fermi liquid semimetal studied by renormalization group analysis, *Phys. Rev. B* **95**, 205106 (2017).
- [6] I. Boettcher and I. F. Herbut, Superconducting quantum criticality in three-dimensional Luttinger semimetals, *Phys. Rev. B* **93**, 205138 (2016).
- [7] I. Mandal, Fate of superconductivity in three-dimensional disordered Luttinger semimetals, *Annals of Physics* **392**, 179 (2018).
- [8] I. Mandal and R. M. Nandkishore, Interplay of Coulomb interactions and disorder in three-dimensional quadratic band crossings without time-reversal symmetry and with unequal masses for conduction and valence bands, *Phys. Rev. B* **97**, 125121 (2018).
- [9] Y.-H. Zhai and J. Wang, Effects of fermion-fermion interactions and impurity scatterings on fermion velocities in the line-nodal superconductors, *The European Physical Journal B* **93**, 86 (2020).
- [10] I. Mandal, Search for plasmons in isotropic Luttinger semimetals, *Annals of Physics* **406**, 173 (2019).
- [11] I. Mandal and H. Freire, Transport in the non-Fermi liquid phase of isotropic Luttinger semimetals, *Phys. Rev. B* **103**, 195116 (2021).
- [12] H. Freire and I. Mandal, Thermoelectric and thermal properties of the weakly disordered non-Fermi liquid phase of Luttinger semimetals, *Physics Letters A* **407**, 127470 (2021).
- [13] I. Mandal and H. Freire, Raman response and shear viscosity in the non-Fermi liquid phase of Luttinger semimetals, *Journal of Physics Condensed Matter* **34**, 275604 (2022).
- [14] I. Mandal, Tunneling in Fermi systems with quadratic band crossing points, *Annals of Physics* **419**, 168235 (2020).
- [15] S. Bera and I. Mandal, Floquet scattering of quadratic band-touching semimetals through a time-periodic potential well, *Journal of Physics: Condensed Matter* **33**, 295502 (2021).
- [16] A. H. Castro Neto, F. Guinea, N. M. R. Peres, K. S. Novoselov, and A. K. Geim, The electronic properties of graphene, *Rev. Mod. Phys.* **81**, 109 (2009).
- [17] D. Yanagishima and Y. Maeno, Metal-nonmetal changeover in pyrochlore iridates, *Journal of the Physical Society of Japan* **70**, 2880 (2001).
- [18] K. Matsuhira, M. Wakeshima, R. Nakanishi, T. Yamada, A. Nakamura, W. Kawano, S. Takagi, and Y. Hinatsu, Metal-Insulator transition in pyrochlore iridates $\text{Ln}_2\text{Ir}_2\text{O}_7$ ($\text{Ln} = \text{Nd}, \text{Sm}, \text{and Eu}$), *Journal of the Physical Society of Japan* **76**, 043706 (2007).
- [19] S. Groves and W. Paul, Band structure of gray tin, *Phys. Rev. Lett.* **11**, 194 (1963).
- [20] Q. Barbedienne, J. Varignon, N. Reyren, A. Marty, C. Vergnaud, M. Jamet, C. Gomez-Carbonell, A. Lemaître, P. Le Fèvre, F. Bertran, A. Taleb-Ibrahimi, H. Jaffrès, J.-M. George, and A. Fert, Angular-resolved photoemission electron spectroscopy and transport studies of the elemental topological insulator $\alpha\text{-Sn}$, *Phys. Rev. B* **98**, 195445 (2018).
- [21] I. M. Tsidilkovski, Band-structure calculation methods, in *Electron Spectrum of Gapless Semiconductors* (Springer, 1997) pp. 3–52.
- [22] J. M. Luttinger, Quantum theory of cyclotron resonance in semiconductors: General theory, *Phys. Rev.* **102**, 1030 (1956).
- [23] A. A. Abrikosov and S. D. Beneslavskii, Possible existence of substances intermediate between metals and dielectrics, in *30 Years of the Landau Institute — Selected Papers*, pp. 64–73.
- [24] S. Murakami, N. Nagosa, and S.-C. Zhang, $\text{SU}(2)$ non-Abelian holonomy and dissipationless spin current in semiconductors, *Phys. Rev. B* **69**, 235206 (2004).
- [25] A. A. Abrikosov, Calculation of critical indices for zero-gap semiconductors, *Sov. Phys.-JETP* **39**, 709 (1974).
- [26] K. Sun, H. Yao, E. Fradkin, and S. A. Kivelson, Topological insulators and nematic phases from spontaneous symmetry breaking in 2D Fermi systems with a quadratic band crossing, *Phys. Rev. Lett.* **103**, 046811 (2009).
- [27] J. M. Murray and O. Vafek, Renormalization group study of interaction-driven quantum anomalous Hall and quantum spin Hall phases in quadratic band crossing systems, *Phys. Rev. B* **89**, 201110 (2014).
- [28] J. W. F. Venderbos, M. Manzardo, D. V. Efremov, J. van den Brink, and C. Ortix, Engineering interaction-induced topological insulators in a $\sqrt{3} \times \sqrt{3}$ substrate-induced honeycomb superlattice, *Phys. Rev. B* **93**, 045428 (2016).
- [29] H.-Q. Wu, Y.-Y. He, C. Fang, Z. Y. Meng, and Z.-Y. Lu, Diagnosis of interaction-driven topological phase via exact diagonalization, *Phys. Rev. Lett.* **117**, 066403 (2016).
- [30] J. Wang, C. Ortix, J. van den Brink, and D. V. Efremov, Fate of interaction-driven topological insulators under disorder, *Phys. Rev. B* **96**, 201104 (2017).
- [31] Y.-M. Dong, Y.-H. Zhai, D.-X. Zheng, and J. Wang, Stability of two-dimensional asymmetric materials with a quadratic band crossing point under four-fermion interaction and impurity scattering, *Phys. Rev. B* **102**, 134204 (2020).
- [32] S. Tchoumakov and W. Witczak-Krempa, Dielectric and electronic properties of three-dimensional Luttinger semimetals with a quadratic band touching, *Phys. Rev. B* **100**, 075104 (2019).
- [33] A. Mauri and M. Polini, Dielectric function and plasmons of doped three-dimensional Luttinger semimetals, *Phys. Rev. B* **100**, 165115 (2019).
- [34] I. F. Herbut, Isospin of topological defects in Dirac systems, *Phys. Rev. B* **85**, 085304 (2012).

- [35] V. Kozii and L. Fu, Thermal plasmon resonantly enhances electron scattering in Dirac/Weyl semimetals, *Phys. Rev. B* **98**, 041109 (2018).
- [36] A. Abrikosov, *Methods of Quantum Field Theory in Statistical Physics*, Dover books on advanced mathematics (Prentice-Hall, 1963).
- [37] G. Mahan, *Many-Particle Physics*, Physics of Solids and Liquids (Springer US, 1990).